

Topological Susceptibility from Slabs

Wolfgang Bietenholz^a, Philippe de Forcrand^{b,c} and Urs Gerber^{a,d}

^a Instituto de Ciencias Nucleares
Universidad Nacional Autónoma de México
A.P. 70-543, C.P. 04510 Distrito Federal, Mexico

^b Institute for Theoretical Physics, ETH Zürich
CH-8093 Zürich, Switzerland

^c CERN, Physics Department, TH Unit
CH-1211 Geneva 23, Switzerland

^d Instituto de Física y Matemáticas
Universidad Michoacana de San Nicolás de Hidalgo
Edificio C-3, Apdo. Postal 2-82
C.P. 58040, Morelia, Michoacán, Mexico

In quantum field theories with topological sectors, a non-perturbative quantity of interest is the topological susceptibility χ_t . In principle it seems straightforward to measure χ_t by means of Monte Carlo simulations. However, for local update algorithms and fine lattice spacings, this tends to be difficult, since the Monte Carlo history rarely changes the topological sector. Here we test a method to measure χ_t even if data from only one sector are available. It is based on the topological charges in sub-volumes, which we denote as slabs. Assuming a Gaussian distribution of these charges, this method enables the evaluation of χ_t , as we demonstrate with numerical results for non-linear σ -models.

1 The topological susceptibility χ_t

There are a number of models in quantum field theory, which have the property that the configurations occur in distinct topological sectors; each sector is characterised by a topological charge $Q \in \mathbb{Z}$. This refers either to infinite volume and configurations with finite actions, or to finite volume with periodic boundary conditions. Here we consider the latter setting, with some volume V in Euclidean space.

The models with this property include in particular 4d $SU(N)$ Yang-Mills theories for all $N \geq 2$. Fermions may be present as well, so this class of models encompasses QCD. In that case, the quenched value of the topological susceptibility χ_t has a prominent application in the explanation of the heavy mass of the pseudo-scalar η' -meson [1].

The measurement of χ_t is a non-perturbative issue, hence lattice simulations are the appropriate method. If the Monte Carlo history changes Q frequently, this measurement is straightforward. However, for most of the popular algorithms, including local update algorithms, as well as the Hybrid Monte Carlo algorithm (which is standard in QCD with dynamical quarks), the auto-correlation time with respect to Q tends to be very long, in particular on fine lattices.¹ This problem is getting even worse in the presence of chiral fermions.

Recently, several indirect methods to measure χ_t nevertheless have been suggested and tested [5, 6]. Here we address a different approach for this purpose, which was first sketched in Ref. [7], but which has not been explored ever since (though a similar approach was studied last year [8]). It is described in Section 2. Sections 3 and 4 give results for the 1d $O(2)$ and the 2d $O(3)$ model, respectively. Our conclusions are discussed in Section 5, and an appendix is devoted to analytical considerations about artifacts in χ_t .

¹In general, the topological sectors are well-defined only in the continuum limit (there are exceptions for lattice actions with a constraint that only admits very smooth configurations [2–4]). So in general transitions are only enabled by lattice artifacts, and by discrete jumps of the algorithm.

2 Evaluating χ_t from slabs

We assume parity symmetry to hold, which implies $\langle Q \rangle = 0$. We further assume the topological charges to obey a Gaussian probability distribution,²

$$p(Q) \propto \exp(-Q^2/(2\chi_t V)) \quad , \quad \chi_t = \frac{1}{V} \langle Q^2 \rangle . \quad (2.1)$$

The idea of the method that we are going to explore, is to divide the periodic volume V into sub-volumes, which we denote as *slabs*, and to extract χ_t from the fluctuations of the topological charge within these slabs. This has the potential of providing the result even based on configurations of a single topological sector (with respect to the entire volume V).

We consider just two slabs, of sizes xV and $(1-x)V$, where $0 < x < 1$.³ At fixed charge Q , we denote the topological charge contribution in the first slab as $q \in \mathbb{R}$; it is obtained by integrating the topological charge density over the slab volume. In general it is not an integer, because not all slab boundaries are periodic. Thus we obtain the probability for the charge contributions q and $Q - q$ in the two slabs,

$$\begin{aligned} p_1(q) \cdot p_2(Q - q)|_{x,V} &\propto \exp\left(-\frac{q^2}{2\chi_t V x}\right) \cdot \exp\left(-\frac{(Q - q)^2}{2\chi_t V (1 - x)}\right) \\ &= \exp\left(-\frac{1}{2\chi_t V} \left[\frac{q'^2}{x(1-x)} + Q^2\right]\right) \\ &\propto \exp\left(-\frac{1}{2\chi_t V} \frac{q'^2}{x(1-x)}\right) , \end{aligned} \quad (2.2)$$

where we defined $q' := q - xQ$.

Eq. (2.2) implies $\langle q \rangle = xQ$, and therefore

$$\langle q'^2 \rangle = \langle q^2 \rangle - x^2 Q^2 . \quad (2.3)$$

Thus, if we measure $\langle q^2 \rangle$ at a set of x values in a fixed sector with topological charge Q , we can fit the results for $\langle q'^2 \rangle$ to the parabola $\chi_t V x(1-x)$, which is predicted by eqs. (2.2) and (2.3).

²The assumption of a Gaussian distribution of the topological charges appears natural in light of instanton gas models. In case of the quantum rotor in infinite volume, it can be demonstrated analytically [9]. Simulations confirm that it also holds — at least to a good approximation — in the 2d $O(3)$ model [6] (cf. Section 4), and in QCD [10].

³The extension of this method to a larger number of slabs is straightforward, but hardly promising, since the slab volumes should not be too small.

The simplest case is the topologically trivial sector, $Q = 0$, where $\langle q^2 \rangle(x) = \langle q'^2 \rangle(x)$ is given by a parabola, which takes its maximum at $x = 1/2$, with a value of $\langle Q^2 \rangle/4$. In the topologically charged sectors, $\langle q'^2 \rangle(x)$ still has the same shape, whereas $\langle q^2 \rangle(x)$ is a parabola that connects $\langle q^2 \rangle(x = 0) = 0$ with $\langle q^2 \rangle(x = 1) = Q^2$. In any sector, the measured data for $\langle q^2 \rangle(x)$ can be fitted to the expected parabola. The susceptibility χ_t is the only fitting parameter, which is evaluated in this manner.

3 Results for the quantum rotor

We first consider a quantum mechanical scalar particle moving freely on a unit circle. We deal with periodic boundary conditions in Euclidean time. Then there is an integer winding number for each trajectory, which characterises the topological sectors of this model. It is also denoted as the 1d $O(2)$ model, or 1d XY model, and it is related to 2d $U(1)$ gauge theory [11].

Now we assume Euclidean time to be uniformly discretised, and on each site $t = 1, 2 \dots L$ there is an angular variable ϕ_t (with $\phi_{t+L} = \phi_t$). We apply the geometric definition of the topological charge Q [12],

$$Q[\phi] = \frac{1}{2\pi} \sum_{t=1}^L \Delta\phi_t \quad , \quad \Delta\phi_t = (\phi_{t+1} - \phi_t) \bmod 2\pi \in (-\pi, \pi] \quad , \quad (3.1)$$

where we define the modulo function such that $\Delta\phi_t$ is the shortest arc length connecting nearest neighbour angular variables.

In our numerical studies we simulated three lattice actions: the standard action, the Manton action [13] and the constraint action [3],⁴

$$\begin{aligned} S_{\text{standard}}[\phi] &= \beta \sum_{t=1}^L \left(1 - \cos(\Delta\phi_t) \right) \\ S_{\text{Manton}}[\phi] &= \frac{\beta}{2} \sum_{t=1}^L (\Delta\phi_t)^2 \\ S_{\text{constraint}}[\phi] &= \begin{cases} 0 & \Delta\phi_t < \delta \quad \forall t \\ +\infty & \text{otherwise.} \end{cases} \end{aligned} \quad (3.2)$$

⁴The constraint action is a special case of a topological lattice action [3, 4, 14], which is characterised by the property that the action remains invariant under most small variations of a configuration.

The continuum limit is attained at $\beta \rightarrow \infty$ or $\delta \rightarrow 0$.

Our simulations were all performed with a cluster algorithm [15]. Due to its non-local update steps, the Markov chain changes the topological sector frequently, which enables a precise direct measurement of the topological susceptibility. This result is then confronted with the value determined by the slab method, described in Section 2.

We begin with an illustration of measured data for the probability product in eq. (2.2), as a function of the relative slab width x (here the “slab” is actually just an interval in Euclidean time).

As a first example, Figure 1 shows data for $\langle q^2 \rangle$, as a function of x . These values were measured with the standard action at size $L = 400$ and $\beta = 4$, which implies a correlation length of $\xi \simeq 6.8$. We see that the curves obtained in the sectors $Q = 0$, $|Q| = 1$ and $|Q| = 2$ do follow the expected parabolas, which interpolate $\langle q^2 \rangle(x = 0) = 0$ and $\langle q^2 \rangle(x = 1) = Q^2$, as predicted in Section 2.

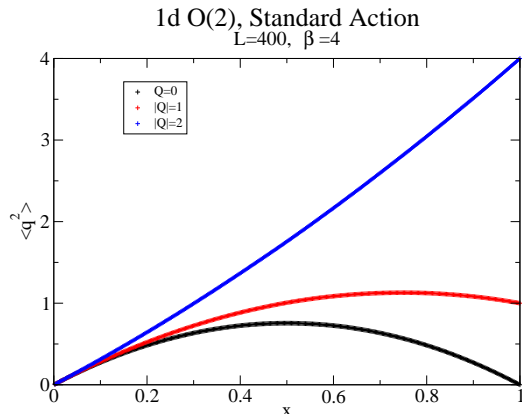


Figure 1: The expectation value $\langle q^2 \rangle(x)$, measured for the standard action at $L = 400$, $\beta = 4$, in the sectors $|Q| = 0, 1, 2$. We confirm the predicted parabolic shape behaviour.

Next we give results obtained with the constraint action, now at $L = 100$ and $\delta = 2\pi/3$, where the correlation length is short, $\xi \simeq 1.1$. Figure 2 shows again the numerical data for $\langle q^2 \rangle$ as a function of x , in the sectors $Q = 0$, $|Q| = 1$ and $|Q| = 2$. For comparison, we also include the parabola for the function $\chi_t V x(1-x)$, which is predicted for $\langle q'^2 \rangle(x)$. Here we insert the directly measured value of χ_t . We see in all cases accurate agreement between this prediction and the numerical data.

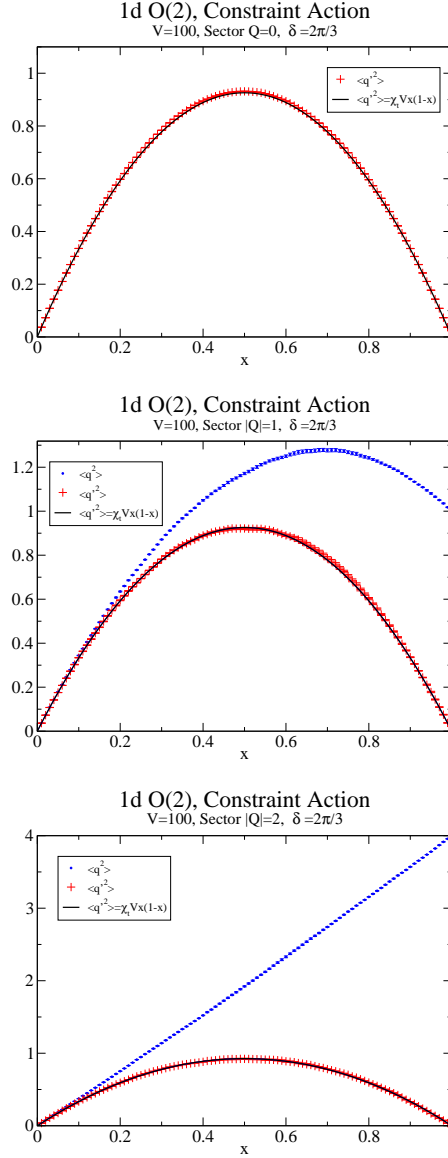


Figure 2: The expectation values $\langle q^2 \rangle(x)$ and $\langle q'^2 \rangle(x)$, measured for the constraint action at $L = 100$, $\delta = 2\pi/3$, in the sectors $|Q| = 0, 1, 2$. For comparison, the black curve shows the predicted behaviour of $\langle q'^2 \rangle(x)$, which agrees very well with the data.

Let us proceed to a quantitative discussion. We start again with the stan-

dard action, where we consider $\beta = 2$ and $\beta = 4$. In a variety of sizes L we applied the slab method, and evaluated χ_t by a fit of the data for $\langle q'^2 \rangle(x)$ to the predicted parabola. The results are given in Table 1. Figure 3 shows the corresponding convergence of the scaling term $\chi_t \xi$, where ξ is the correlation length.⁵ They are consistently close to the analytical value at infinite L (the corresponding formula is given in Ref. [9]). That value is in all cases compatible with the directly measured χ_t , which is also included in Table 1. For increasing L the agreement with the slab method results improves further.

L	direct	$Q = 0$	$ Q = 1$	$ Q = 2$
$\beta = 2$ $\chi_{t,L=\infty} = 0.019364$ $\xi = 2.778866$				
100	0.019369(6)	0.019280(7)	0.019324(11)	0.019480(29)
200	0.019372(8)	0.019346(14)	0.019314(10)	0.019326(19)
400	0.019365(10)	0.019348(16)	0.019337(11)	0.019333(19)
$\beta = 4$ $\chi_{t,L=\infty} = 0.007554$ $\xi = 6.814998$				
150	0.007554(3)	0.007534(4)	0.007550(6)	0.007587(2)
200	0.007557(3)	0.007541(3)	0.007547(4)	0.007581(8)
250	0.007549(3)	0.007542(3)	0.007550(4)	0.007585(8)
300	0.007560(4)	0.007545(3)	0.007545(5)	0.007554(5)
350	0.007554(5)	0.007545(4)	0.007557(2)	0.007553(5)
400	0.007549(5)	0.007552(4)	0.007551(3)	0.007564(5)

Table 1: Explicit results for χ_t by the slab method, for the standard action at $\beta = 2$ and $\beta = 4$, as illustrated in Figure 3.

Next we give analogous results for the Manton action, Figure 4 and Table 2, and for the constraint action, Figure 5 and Table 3. Qualitatively the same features are confirmed. Quantitatively we see that the Manton action — which is classically perfect [9] — performs very well regarding the convergence towards the value at $L = \infty$. For all actions, the convergence is best for $|Q| \leq 1$, while $|Q| = 2$ is affected by somewhat stronger finite size effects.

⁵Here and in Figures 2 and 5 we insert the analytic values for ξ , which are also given in Tables 1, 2 and 3. They were calculated with the formulae given in Refs. [9] and [3] as functions of β and δ , see also Tables 1, 2 and 3. This refers to $L \rightarrow \infty$, but since $L \gg \xi$ holds in all cases, this is not problematic.

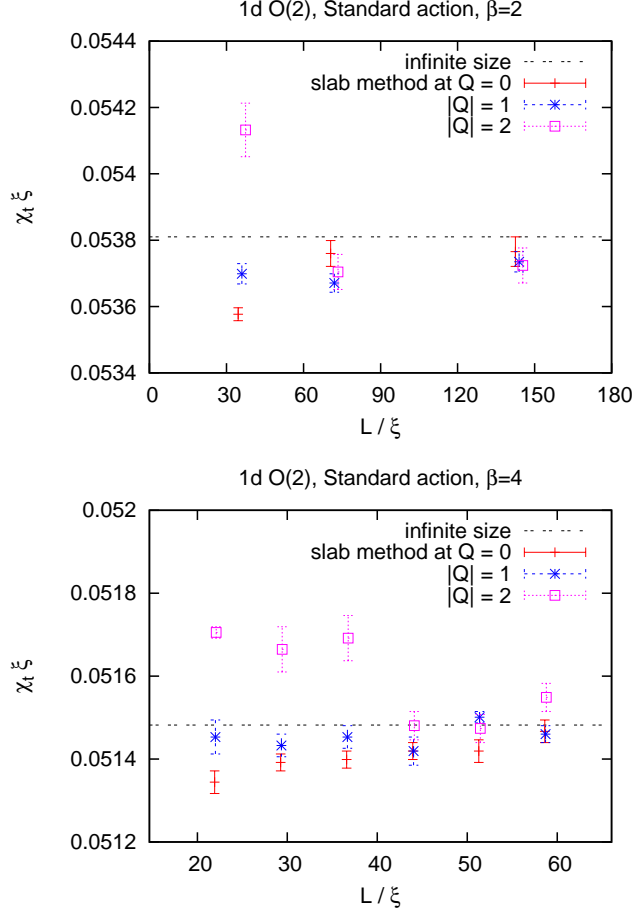


Figure 3: The results for χ_t , in units of $1/\xi$, based on the slab method, for the standard action at $\beta = 2$ (above) and $\beta = 4$ (below). For an increasing ratio L/ξ they move towards the analytic result in the thermodynamic limit (dashed line).

We also verified that $\langle Q \rangle$ and the kurtosis term (which is related to the Binder cumulant),

$$c_4 = \frac{1}{V} \left(3\langle Q^2 \rangle^2 - \langle Q^4 \rangle \right), \quad (3.3)$$

are both compatible with 0 in all cases (within at most 2σ).⁶ The former

⁶For these parameters and huge statistics of $O(10^9)$ measurements, the error in c_4 can be reduced to $O(10^{-5})$, and one observes significant deviations from zero [6]. However,

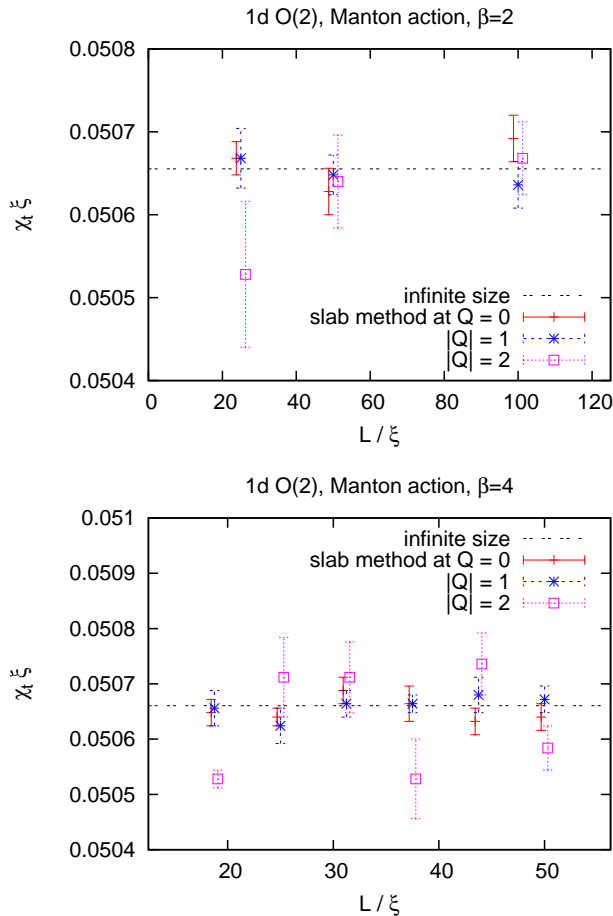


Figure 4: Results for χ_t , in units of $1/\xi$, based on the slab method, for the Manton action at $\beta = 2$ (above) and $\beta = 4$ (below). Compared to the standard action, a significantly smaller ratio L/ξ is sufficient for a very good approximation to the infinite size result (dashed line).

follows from parity symmetry, and a Gaussian Q -distribution implies $c_4 = 0$. The vanishing of these two quantities is an assumption of the slab method. For the kurtosis this condition is not trivial; it will be considered in detail in the next section.

Another source of systematic errors are artifacts in χ_t due to the finite size and finite lattice spacing. These artifacts are discussed in Appendix A.

these tiny c_4 values have no influence on the interpretation of the results presented here.

L	direct	$Q = 0$	$ Q = 1$	$ Q = 2$
$\beta = 2$ $\chi_{t,L=\infty} = 0.012663$ $\xi = 4.000321$				
100	0.012658(7)	0.012666(5)	0.012666(9)	0.012631(22)
200	0.012661(4)	0.012656(7)	0.012661(6)	0.012659(14)
400	0.012653(4)	0.012672(7)	0.012658(7)	0.012666(11)
$\beta = 4$ $\chi_{t,L=\infty} = 0.006333$ $\xi = 8.000000$				
150	0.006330(4)	0.006331(3)	0.006332(4)	0.006316(2)
200	0.006333(3)	0.006330(2)	0.006328(4)	0.006339(9)
250	0.006335(3)	0.006336(3)	0.006333(3)	0.006339(8)
300	0.006332(3)	0.006333(4)	0.006333(2)	0.006316(9)
350	0.006334(4)	0.006329(3)	0.006335(4)	0.006342(7)
400	0.006329(3)	0.006330(3)	0.006334(3)	0.006323(5)

Table 2: Explicit results for χ_t by the slab method, for the Manton action at $\beta = 2$ and $\beta = 4$, as illustrated in Figure 4.

L	direct	$Q = 0$	$ Q = 1$	$ Q = 2$
$\delta = 2\pi/3$ $\chi_{t,L=\infty} = 0.037037$ $\xi = 1.132367$				
100	0.037036(13)	0.037281(16)	0.037183(14)	0.036990(35)
200	0.037008(15)	0.037163(20)	0.037121(18)	0.037079(29)
400	0.037042(19)	0.037091(33)	0.037109(23)	0.037056(26)
$\delta = 1.5$ $\chi_{t,L=\infty} = 0.018998$ $\xi = 2.451141$				
100	0.018987(8)	0.019113(8)	0.019058(10)	0.018864(28)
200	0.019011(9)	0.019050(9)	0.019049(13)	0.018983(17)
400	0.018992(7)	0.019038(13)	0.019032(8)	0.019019(12)
$\delta = 1$ $\chi_{t,L=\infty} = 0.008443$ $\xi = 5.793617$				
100	0.008443(5)	0.008491(3)	0.008416(10)	0.008208(36)
200	0.008445(4)	0.008475(5)	0.008452(7)	0.008397(16)
400	0.008439(5)	0.008460(5)	0.008455(6)	0.008445(15)

Table 3: Explicit results for χ_t by the slab method, for the constraint action at $\delta = 2\pi/3$, 1.5 and 1, as illustrated in Figure 5.

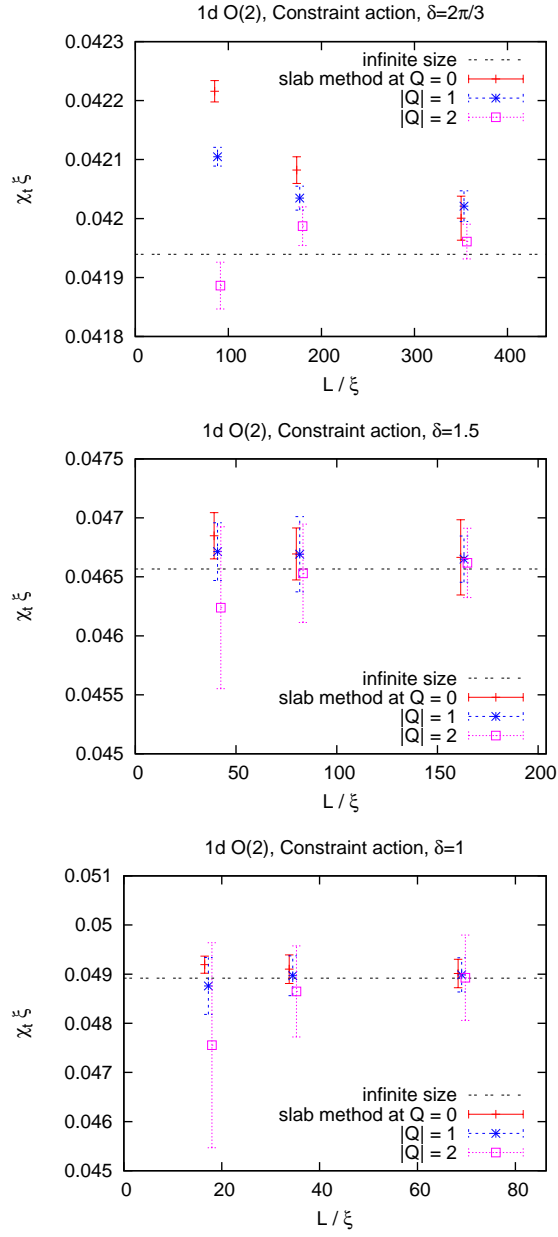


Figure 5: Results for χ_t , in units of $1/\xi$, based on the slab method, for the constraint action at $\delta = 2\pi/3, 1.5$ and 1 , as a function of L/ξ .

4 Results for the 2d Heisenberg model

We proceed to the 2d $O(3)$ model, where we consider square lattices with classical spins $\vec{e}_x \in S^2$ on the sites x . In order to define the topological charge, we cut each plaquette into two triangles (with an alternating orientation between adjacent plaquettes). For a triangle with sites x, y, z we identify the (minimal) solid angle spanned by $\vec{e}_x, \vec{e}_y, \vec{e}_z$, including a sign factor for its orientation (a fully explicit description is given in Ref. [3]).

The sum of the two oriented solid angles within a plaquette, divided by 4π , defines the topological charge density q_x . The total charge of a spin configuration $[\vec{e}]$ amounts to $Q[\vec{e}] = \sum_x q_x \in \mathbb{Z}$. It counts how many times the sum of these solid angles covers the sphere S^2 with a definite orientation.

In analogy to Section 3, we consider three lattice actions, including an obvious generalisation of the Manton action, which was simulated with a new variant of the Wolff cluster algorithm,

$$\begin{aligned}
 S_{\text{standard}}[\vec{e}] &= \beta \sum_{x,\mu=1,2} (1 - \vec{e}_x \cdot \vec{e}_{x+\hat{\mu}}) \\
 S_{\text{Manton}}[\vec{e}] &= \beta \sum_{x,\mu=1,2} \left(1 - [\arccos(\vec{e}_x \cdot \vec{e}_{x+\hat{\mu}})]^2 \right) \\
 S_{\text{constraint}}[\vec{e}] &= \begin{cases} 0 & \vec{e}_x \cdot \vec{e}_{x+\hat{\mu}} > \cos \delta \quad \forall x, \mu = 1, 2 \\ +\infty & \text{otherwise.} \end{cases} \quad (4.1)
 \end{aligned}$$

Regarding the application of the slab method with these lattice actions, Figure 6 shows results obtained in the lattice volumes $V = 48^2$ and 64^2 .

We also consider further volumes, including rectangular shapes. In fact, it is not obvious if the slab method results should be compared to χ_t in the entire (periodic) volume V , or to $\chi_{t,V/2}$ in a (non-periodic) slab of size $V/2$. Hence we have measured the latter as well, for comparison. The detailed results, along with the corresponding correlation length, are given in Tables 4, 5 and 6.⁷ However, for volumes, which are large enough for the slab method to work quite well, it turns out that χ_t and $\chi_{t,V/2}$ are too close to each other to be distinguished in light of the slab method results.

The assumption of a Gaussian distribution of the topological charges is essential for the viability of this method. Figure 7 shows that the kurto-

⁷In this model, the apparent scaling quantity $\chi_t \xi^2$ diverges logarithmically in the continuum limit (see *e.g.* Ref. [3]), so here we refer directly to χ_t .

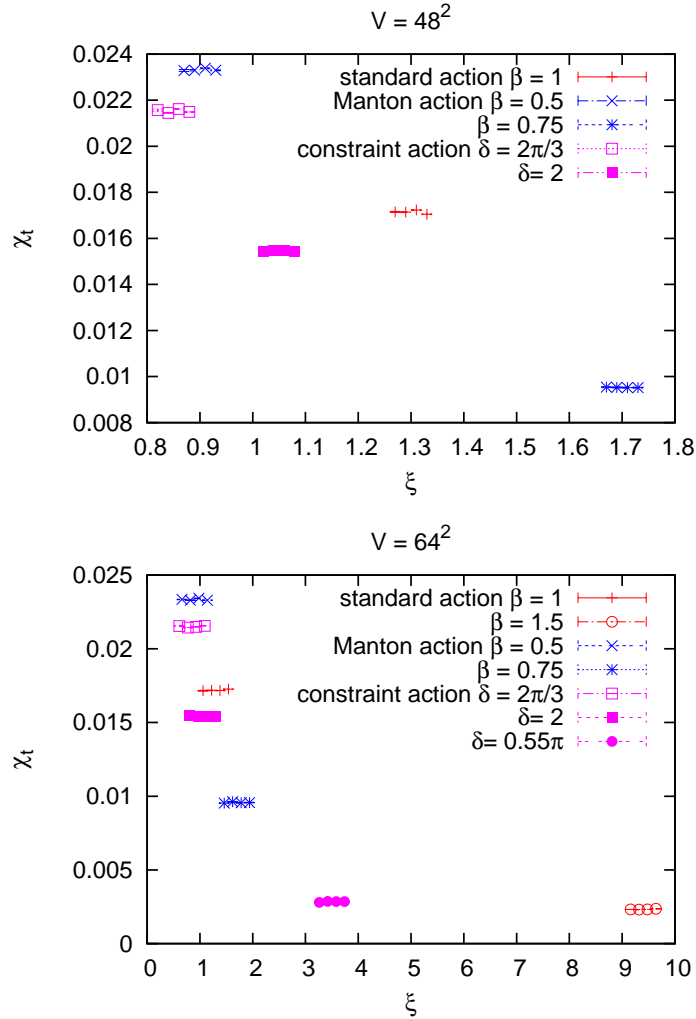


Figure 6: Results for the topological susceptibility χ_t in the 2d $O(3)$ model, in the volumes $V = 48^2$ and 64^2 , for three lattice actions. Each set of results consists of four data points and shows (from left to right) the directly measured value, and the results by the slab method in the sectors $|Q| = 0, 1, 2$.

sis (3.3) — as a measure for the deviation from a Gaussian — decreases rapidly as we approach the continuum limit; for the Manton action we see an exponential decrease of $|c_4|$ as ξ increases. Thus a non-zero value of $|c_4|$ appears as a lattice artifact, and not as a finite size effect; this observation

β	V	χ_t^{direct}	$\chi_{t,V/2}^{\text{direct}}$	$\chi_t^{Q=0}$	$\chi_t^{ Q =1}$	$\chi_t^{ Q =2}$
1	48^2	0.01715(2)	0.01718(2)	0.01714(2)	0.01723(2)	0.01705(2)
	64^2	0.01716(3)	0.01717(2)	0.01718(2)	0.01717(2)	0.01726(2)
1.5	64^2	0.002319(3)	0.002354(2)	0.002305(5)	0.002322(5)	0.002361(5)
	80^2	0.002332(5)	0.002356(3)	0.002327(4)	0.002327(4)	0.002358(4)
	64×128	0.002332(4)	0.002344(3)	0.002304(3)	0.002321(2)	0.002324(3)
	96^2	0.002341(3)	0.002359(3)	0.002333(3)	0.002337(3)	0.002352(3)
	128^2	0.002327(3)	0.002347(3)	0.002390(10)	0.002381(9)	0.002371(9)
	128×256	0.002334(4)	0.002342(3)	0.002353(1)	0.002351(1)	0.002366(1)

Table 4: Results for the topological susceptibility χ_t in the 2d $O(3)$ model with the standard action. We consider a variety of volumes at $\beta = 1$ and at $\beta = 1.5$, with a correlation length of $\xi = 1.3$ and 9.4 , respectively. The results for $V = 48^2$ and 64^2 are illustrated in Figure 6.

β	V	χ_t^{direct}	$\chi_{t,V/2}^{\text{direct}}$	$\chi_t^{Q=0}$	$\chi_t^{ Q =1}$	$\chi_t^{ Q =2}$
0.5	48^2	0.02329(4)	0.02333(3)	0.02330(3)	0.02339(2)	0.02330(2)
	64^2	0.02335(2)	0.02335(3)	0.02330(2)	0.02343(2)	0.02330(2)
0.75	48^2	0.00954(2)	0.00956(1)	0.00953(2)	0.00952(2)	0.00952(2)
	64^2	0.00953(2)	0.00957(1)	0.00962(2)	0.00955(1)	0.00957(2)

Table 5: Results for the topological susceptibility χ_t in the 2d $O(3)$ model with the Manton action. We consider two volumes at $\beta = 0.5$ and at $\beta = 0.75$, with a correlation length of $\xi = 0.9$ and 1.7 , respectively. These results are illustrated in Figure 6.

agrees qualitatively with a discussion in Ref. [6]. This artifact is much less suppressed for the standard action and the constraint action. Regarding the application of the slab method with these lattice actions, Figure 6 shows results obtained in the lattice volume $V = 48^2$ and 64^2 . The systematic errors of the slab method appear as tiny deviations of χ_t extracted from $|Q| = 0, 1$ and 2 (three rightmost points in each set of four) from the directly measured value (leftmost point).

δ	V	χ_t^{direct}	$\chi_{t, V/2}^{\text{direct}}$	$\chi_t^{Q=0}$	$\chi_t^{ Q =1}$	$\chi_t^{ Q =2}$
$2\pi/3$	48^2	0.02157(5)	0.02155(2)	0.02145(2)	0.02162(2)	0.02149(2)
	64^2	0.02144(4)	0.02151(3)	0.02144(2)	0.02149(2)	0.02156(2)
2	48^2	0.01545(2)	0.01547(2)	0.01549(2)	0.01546(1)	0.01543(2)
	64^2	0.01549(3)	0.01547(2)	0.01538(2)	0.01541(1)	0.01543(1)
0.55π	16^2	0.002445(6)	0.002663(4)	0.002168(65)	0.003806(14)	0.005211(27)
	32^2	0.002795(4)	0.002873(3)	0.002816(17)	0.002888(16)	0.003146(15)
	64^2	0.002797(4)	0.002835(4)	0.002859(6)	0.002853(7)	0.002850(7)
	64×128	0.002795(4)	0.002816(3)	0.002826(3)	0.002812(3)	0.002810(3)
	96^2	0.002792(5)	0.002818(3)	0.002831(4)	0.002835(4)	0.002843(4)
	128^2	0.002783(6)	0.002805(3)	0.002837(3)	0.002828(3)	0.002819(3)

Table 6: Results for the topological susceptibility χ_t in the 2d $O(3)$ model with the constraint action. We consider a variety of volumes at $\delta = 2\pi/3$, 2 and 0.55π , with a correlation length of $\xi = 0.85$, 1.05 and 3.5, respectively. The results for $V = 48^2$ and 64^2 are illustrated in Figure 6.

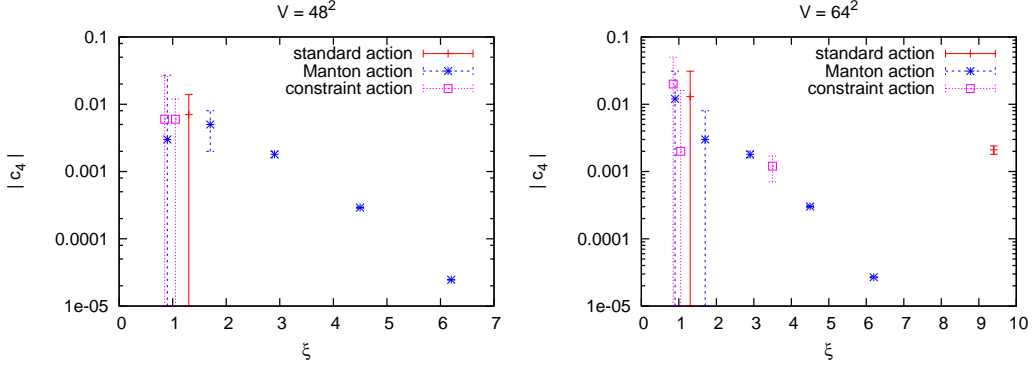


Figure 7: The absolute value of the kurtosis, given in eq. (3.3), in the 2d $O(3)$ model. For each of the three actions, and at a fixed correlation length ξ , we display the results in $V = 48^2$ (on the left), and $V = 64^2$ (on the right). We see that the volume hardly affects the value of $|c_4|$, which decreases for increasing correlation length ξ . This convergence to zero is fastest for the Manton action, where we recognise an exponential decrease.

5 Conclusions

We have tested an unconventional method for the numerical measurement of the topological susceptibility χ_t , based on the division of the volume into slabs. This method is applicable even if configurations in only one topological sector are available.

Our study shows that — under suitable conditions — this method works very well. Its statistical accuracy is comparable to the precision in the absence of “topological slowing down”, *i.e.* the slab method is not affected by the freezing of the topological sectors.

In particular, we obtained in the 2d $O(3)$ model results for χ_t , which are correct on the percent level, and in the 1d $O(2)$ far beyond. This precision was revealed by large statistics of $O(10^7)$ measurements, which would not be accessible in higher dimensional models like QCD; in this sense, the accuracy of the slab results are fully satisfactory.

The slab method is most successful at small topological charges, $|Q| \leq 1$, whereas its application in the sector $|Q| = 2$ is more tedious, since the finite size effects are worse. However, even at $|Q| \leq 1$ the finite size effects are highly persistent. In fact, other methods and formulae show that these effects are only suppressed by a power series in $1/V$ for topologically fixed measurements [5, 6].

As an illustrative example of possible systematic effects, we refer to the results at $\delta = 0.55\pi$ in Table 6: even the smallest volume, $V = 16^2$, corresponds to the ratio $L/\xi \simeq 4.6$, where one would expect usual (*i.e.* exponentially suppressed) finite size effects to be mostly eliminated. The results for the slab method, however, are strongly distorted — they improve significantly at $L = 32$ (and for $|Q| = 2$ it even takes $L = 64$).

This illustrates the general feature: at fixed β or δ , *i.e.* at approximately constant ξ , the slab results converge for increasing volume. In order to assure that they do converge to the (vicinity of the) correct value, we further have to require the topological charges Q to be (approximatively) Gauss-distributed (that also ensures a good fit to formula 2.2). Therefore we also studied the kurtosis, which may deviate from zero (indicating a deviation from a Gaussian) as a lattice artifact. It is suppressed when ξ increases (in lattice units), with a rate that depends on the lattice action; for the Manton action we observed a particularly fast, exponential suppression.

Hence ξ should be sufficiently large to control that requirement, and the volume should be large enough to obtain $L/\xi = O(10)$; then the slab method

can be expected to provide the correct χ_t value on the percent level.

Acknowledgements

We thank Irais Bautista and Christoph P. Hofmann for inspiring discussions. This work was supported in part by the Mexican *Consejo Nacional de Ciencia y Tecnología* (CONACYT) through projects CB-2010/155905 and CB-2013/222812, and by DGAPA-UNAM, grant IN107915.

A Artifacts in the topological susceptibility

An essential point for the quality of the results obtained by the slab method is the precision of χ_t as measured in the sub-volumes. In this appendix we discuss the artifacts that occur: Sub-Appendix A.1 deals with the finite size effects, which depend on the ratio ξ/L , and which even occur in the continuum formulation. Sub-Appendix A.2 considers the lattice artifacts, as a function of a/L (where a is the lattice spacing, and L is now the dimensional size). Both considerations are performed in the analytically tractable case of the quantum rotor; Sub-Appendix A.2 captures the standard and the Manton action. For simplicity we deal with periodic boundary conditions throughout, although they are partly open in the sub-volumes, so we assume implicitly that L is large enough for this distinction to be negligible.

A.1 Finite size effects

While the slab method is plagued by particularly persistent finite size effects, the true χ_t value tends to converge exponentially as the volume is enlarged. Here we discuss this convergence for the case of the 1d $O(2)$ model.

In the continuum formulation, with the action $S[\varphi] = \frac{\beta}{2} \int_0^L \dot{\varphi}^2 dt$, the topological susceptibility takes the form [9]

$$\chi_t = \frac{1}{L} \langle Q^2 \rangle = \frac{1}{L} \frac{\sum_{Q \in \mathbb{Z}} Q^2 e^{-\alpha \pi Q^2}}{\sum_{Q \in \mathbb{Z}} e^{-\alpha \pi Q^2}}, \quad \alpha := 2\pi\beta/L. \quad (\text{A.1})$$

It can be written in terms of a Jacobi θ -function,

$$\chi_t = -\frac{1}{\pi L} \frac{d}{d\alpha} \ln \theta(\alpha), \quad \theta(\alpha) := \sum_{Q \in \mathbb{Z}} e^{-\alpha \pi Q^2}. \quad (\text{A.2})$$

By applying the Jacobi identity,

$$\theta(\alpha) = \frac{1}{2\pi\sqrt{\alpha}} \theta(1/\alpha) , \quad (\text{A.3})$$

we obtain

$$\theta(\alpha)|_{0<\alpha\ll 1} \simeq \frac{1}{2\pi\sqrt{\alpha}} \left(1 + 2e^{-\pi/\alpha} + 2e^{-4\pi/\alpha} \dots \right) . \quad (\text{A.4})$$

Inserting approximation (A.4) into formula (A.2), we arrive at

$$\chi_t \simeq \frac{1}{(2\pi)^2\beta} + \frac{L}{2\pi^2\beta^2} \left(-e^{-L/(2\beta)} + e^{-L/\beta} \right) . \quad (\text{A.5})$$

With the correlation length $\xi = 2\beta$ [9], this corresponds to the ratio

$$\frac{\chi_t}{\chi_{t, L=\infty}} \simeq 1 + \frac{4L}{\xi} \left(-e^{-L/\xi} + e^{-2L/\xi} \right) . \quad (\text{A.6})$$

Thus we see explicitly the exponentially suppressed finite size corrections. Figure 8 illustrates this formula, and compares it to the exact result (numerical summation of the series in eq. (A.1)), which agrees with simulation data for the Manton action at $\beta = 4$ (where lattice artifacts are practically erased).

A.2 Lattice artifacts

We begin with general properties of a field theory in a periodic Euclidean volume V , where the configurations of the field ϕ are divided into topological sectors. In presence of a vacuum angle θ (and with $\hbar = 1$), the partition function and the topological susceptibility can be written as⁸

$$Z(\theta) = \int D\phi e^{-S[\phi] - iQ[\phi]\theta} , \quad \chi_t = \frac{1}{V} \left[-\frac{Z''}{Z} + \left(\frac{Z'}{Z} \right)^2 \right] . \quad (\text{A.7})$$

In the Hamilton formulation, the partition function reads

$$Z(\theta) = \text{Tr} e^{-\beta\hat{H}(\theta)} = \sum_n e^{-\beta E_n(\theta)} ,$$

⁸Occasionally we omit the argument θ in the partition function and (below) in the energy eigenvalues.

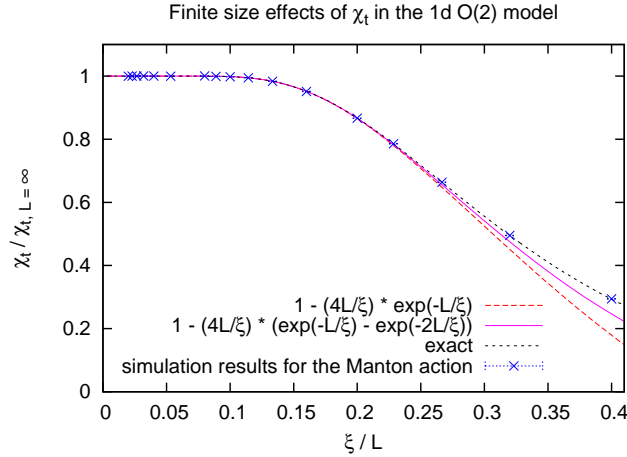


Figure 8: The ratio $\chi_t/\chi_{t,L=\infty}$ as a function of ξ/L . We show the leading and next-to-leading finite size correction in approximation (A.6), the exact result and simulations results for the Manton action at $\beta = 4$.

where β is the inverse temperature, and we assume a discrete energy spectrum. Inserting eq. (A.7) leads to

$$\chi_t = \frac{1}{Z} \frac{\beta}{V} \sum_n [E_n'' - \beta(E_n')^2] e^{-\beta E_n} + \frac{1}{Z^2} \frac{\beta^2}{V} \left(\sum_n E_n' e^{-\beta E_n} \right)^2. \quad (\text{A.8})$$

Now we focus on $d = 1$, and replace V and β both by L (the periodicity range in Euclidean time). More specifically, we consider again the quantum rotor, where L also represents the moment of inertia. We deal with a lattice of spacing a , and periodicity over N sites, $L = Na$. A consideration of the transfer matrix yields [9]

$$e^{-aE_n} = \sqrt{\frac{L}{2\pi a}} \int_{-\pi}^{\pi} d\varphi \exp\left(-\frac{L}{a}f(\varphi) - i\left(n - \frac{\theta}{2\pi}\right)\varphi\right) \doteq \sqrt{\frac{L}{2\pi a}} I_n(\theta),$$

where $n \in \mathbb{Z}$, and

$$f(\varphi) = \begin{cases} 1 - \cos \varphi & \text{standard action} \\ \frac{1}{2}\varphi^2 & \text{Manton action.} \end{cases}$$

In either case, $f(\varphi)$ is even, such that $E_n'(0) = 0$, in accordance with $\langle Q \rangle_{\theta=0} =$

0, and some algebra leads to

$$\chi_{t,\theta=0} = \frac{1}{a} \frac{\sum_n [-I_n'' I_n + (N+1)(I_n')^2] I_n^{N-2}}{\sum_m I_m^N} \Big|_{\theta=0},$$

with

$$I_n(0) = \int_{-\pi}^{\pi} d\varphi e^{-f(\varphi)L/a} \cos(n\varphi)$$

$$I_n'(0) = \frac{1}{2\pi} \int_{-\pi}^{\pi} d\varphi e^{-f(\varphi)L/a} \varphi \sin(n\varphi)$$

$$I_n''(0) = -\frac{1}{(2\pi)^2} \int_{-\pi}^{\pi} d\varphi e^{-f(\varphi)L/a} \varphi^2 \cos(n\varphi). \quad (\text{A.9})$$

To proceed, we now have to specify $f(\varphi)$. We start with the *Manton action*, and substitute $\bar{\varphi} \doteq \varphi\sqrt{N}$,

$$I_n(0) = \frac{1}{\sqrt{N}} \int_{-\pi\sqrt{N}}^{\pi\sqrt{N}} d\bar{\varphi} e^{-\bar{\varphi}^2/2} \cos(n\bar{\varphi}/\sqrt{N}) \doteq \frac{1}{\sqrt{N}} J_n^{(0)}$$

$$I_n'(0) = \frac{1}{2\pi N} \int_{-\pi\sqrt{N}}^{\pi\sqrt{N}} d\bar{\varphi} e^{-\bar{\varphi}^2/2} \bar{\varphi} \sin(n\bar{\varphi}/\sqrt{N}) \doteq \frac{1}{2\pi N} J_n^{(1)}$$

$$I_n''(0) = -\frac{1}{(2\pi)^2 N^{3/2}} \int_{-\pi\sqrt{N}}^{\pi\sqrt{N}} d\bar{\varphi} e^{-\bar{\varphi}^2/2} \bar{\varphi}^2 \cos(n\bar{\varphi}/\sqrt{N}) \doteq \frac{1}{(2\pi)^2 N^{3/2}} J_n^{(2)}$$

$$\chi_{t,\theta=0}^{\text{Manton}} = \frac{1}{(2\pi)^2 LN} \frac{\sum_n [-J_n^{(2)} J_n^{(0)} + (N+1)(J_n^{(1)})^2] (J_n^{(0)})^{N-2}}{\sum_m (J_m^{(0)})^N}. \quad (\text{A.10})$$

If we write $\cos(n\bar{\varphi}/\sqrt{N})$ and $\sin(n\bar{\varphi}/\sqrt{N})$ in exponential form, and complete the squares in the exponents,

$$-\frac{1}{2}\bar{\varphi}^2 + in\bar{\varphi}/\sqrt{N} = -\frac{1}{2}(\bar{\varphi} - in/\sqrt{N})^2 - \frac{n^2}{2N}, \quad (\text{A.11})$$

we see several types of lattice artifacts, such as the extra term $-n^2/(2L)$ in the exponent, and the incomplete Gauss integrals; they are *exponentially suppressed* in a/L . The substitution of the integration variable $\bar{\varphi} \rightarrow \bar{\varphi} - in/\sqrt{N}$ corresponds to a shift of the integration contour; for the incomplete Gauss integral this is another artifact, which is exponentially suppressed. In summary, there are no power lattice artifacts for the Manton action.

For the *standard action* the corresponding formulae read

$$\chi_{t,\theta=0}^{\text{standard}} = \frac{1}{(2\pi)^2 a} \frac{\sum_n [\tilde{I}_n^{(2)} \tilde{I}_n^{(0)} + (N+1)(\tilde{I}_n^{(1)})^2] (\tilde{I}_n^{(0)})^{N-2}}{\sum_m (\tilde{I}_m^{(0)})^N},$$

with

$$\begin{aligned} \tilde{I}_n^{(0)} &\doteq \int_{-\pi}^{\pi} d\varphi e^{(\cos \varphi - 1)N} \cos(n\varphi) \\ \tilde{I}_n^{(1)} &= \int_{-\pi}^{\pi} d\varphi e^{(\cos \varphi - 1)N} \varphi \sin(n\varphi) \\ \tilde{I}_n^{(2)} &= \int_{-\pi}^{\pi} d\varphi e^{(\cos \varphi - 1)N} \varphi^2 \cos(n\varphi). \end{aligned} \quad (\text{A.12})$$

Regarding the search for *power lattice artifacts*, we start from the Manton action and add the two leading modifications of the standard action, $f(\varphi) \simeq \varphi^2/2 - \varphi^4/4! + \varphi^6/6!$. This modifies the expressions for $I_n(0)$, $I'_n(0)$ and $I''_n(0)$ in eq. (A.10) by a factor

$$\left(1 + \frac{1}{4!N} \bar{\varphi}^4 + \frac{1}{2(4!N)^2} \bar{\varphi}^8 - \frac{1}{6!N^2} \bar{\varphi}^6\right)$$

under the integrals, and after some calculus we obtain

$$\chi_{t,\theta=0}^{\text{standard}} \simeq \chi_{t,\theta=0}^{\text{Manton}} \left(1 + \frac{a}{2L} + \frac{13}{24} \frac{a^2}{L^2}\right). \quad (\text{A.13})$$

Hence for the standard action $\chi_{t,\theta=0}$ is affected by corrections linear in a/L .

This may appear surprising for a bosonic theory, but one has to keep in mind that $\chi_{t,\theta=0}$ is not a scaling quantity. The actual scaling artifacts refer to the product $\chi_t \xi$. In the thermodynamic limit they are expressed in powers of a/ξ [3],

$$\chi_t \xi = \begin{cases} \frac{1}{2\pi^2} \left(1 + \frac{1}{3} \frac{a^2}{\xi^2} \dots\right) & \text{standard action} \\ \frac{1}{2\pi^2} \left(1 - \sqrt{\pi \xi} a (1 - 4/\pi^2) e^{-\pi^2 \xi / (4a)} + \dots\right) & \text{Manton action} \\ \frac{1}{2\pi^2} \left(1 - \frac{1}{5} \frac{a}{\xi} + \dots\right) & \text{constraint action.} \end{cases}$$

For the standard action, the linear artifacts cancel in this scaling quantity, while the Manton action is classically perfect; its scaling artifacts are exponentially suppressed. As an exotic feature, the constraint action does have linear artifacts, due to the absence of a derivative term in the action.

We summarise that the finite size effects are exponentially suppressed in L/ξ , whereas the type of lattice artifacts depend on the lattice action.

References

- [1] E. Witten, *Nucl. Phys. B* **156** (1979) 269. G. Veneziano, *Nucl. Phys. B* **159** (1979) 213.
- [2] M. Lüscher, *Nucl. Phys. B* **549** (1999) 295 [hep-lat/9811032].
- [3] W. Bietenholz, U. Gerber, M. Pepe and U.-J. Wiese, *JHEP* **12** (2010) 020 [arXiv:1009.2146 [hep-lat]].
- [4] O. Akerlund and P. de Forcrand *JHEP* **1506** (2015) 183 [arXiv:1505.02666 [hep-lat]].
- [5] R. Brower, S. Chandrasekharan, J.W. Negele and U.-J. Wiese, *Phys. Lett. B* **560** (2003) 64 [hep-lat/0302005].
S. Aoki, H. Fukaya, S. Hashimoto and T. Onogi, *Phys. Rev. D* **76** (2007) 054508 [arXiv:0707.0396 [hep-lat]].
S. Aoki *et al.* (JLQCD and TWQCD Collaborations), *Phys. Lett. B* **665** (2008) 294 [arXiv:0710.1130 [hep-lat]].
W. Bietenholz, I. Hip, S. Shcheredin and J. Volkholz, *Eur. Phys. J. C* **72** (2012) 1938 [arXiv:1109.2649 [hep-lat]].
A. Dromard and M. Wagner, *Phys. Rev. D* **90** (2014) 074505 [arXiv:1404.0247 [hep-lat]].
H. Fukaya, S. Aoki, G. Cossu, S. Hashimoto, T. Kaneko and J. Noaki (JLQCD Collaboration), arXiv:1411.1473 [hep-lat].
- [6] I. Bautista, W. Bietenholz, A. Dromard, U. Gerber, C.P. Hofmann, H. Mejía-Díaz and M. Wagner, arXiv:1503.06853 [hep-lat].
- [7] P. de Forcrand, M. García Pérez, J.E. Hetrick, E. Laermann, J.F. Lagae and I.O. Stamatescu, *Nucl. Phys. Proc. Suppl.* **73** (1999) 578 [hep-lat/9810033].
- [8] R.C. Brower *et al.* (LSD Collaboration), *Phys. Rev. D* **90** (2014) 014503 [arXiv:1403.2761 [hep-lat]].
- [9] W. Bietenholz, R. Brower, S. Chandrasekharan and U.-J. Wiese, *Phys. Lett. B* **407** (1997) 283 [hep-lat/9704015].
- [10] S. Dürr, Z. Fodor, C. Hoelbling and T. Kurth, *JHEP* **0704** (2007) 055 [hep-lat/0612021].

- [11] R. Sinclair, *Phys. Rev.* **D 45** (1992) 2098.
- [12] B. Berg and M. Lüscher, *Nucl. Phys.* **B 190** (1981) 412.
- [13] N. Manton, *Phys. Lett.* **B 96** (1980) 328.
- [14] W. Bietenholz, M. Bögli, F. Niedermayer, M. Pepe, F.G. Rejón-Barrera and U.J. Wiese, *JHEP* **1303** (2013) 141 [arXiv:1212.0579 [hep-lat]].
W. Bietenholz, U. Gerber and F.G. Rejón-Barrera, *J. Stat. Mech.* (2013) P12009 [arXiv:1307.0485 [hep-lat]].
- [15] U. Wolff, *Phys. Rev. Lett.* **62** (1989) 361.